

Investigating Dark Matter and MOND Models with Galactic Rotation Curve Data

Mads T. Frandsen* and Jonas Petersen†

*CP³-Origins, University of Southern Denmark,
Campusvej 55, DK-5230 Odense M, Denmark*

(Dated: February 19, 2024)

Abstract

We study geometries of galactic rotation curves from Dark Matter (DM) and Modified Newtonian Dynamics (MOND) models in $(g_{\text{bar}}, g_{\text{tot}})$ -space (g_2 -space) where g_{tot} is the total centripetal acceleration of matter in the galaxies and g_{bar} is that due to the baryonic (visible) matter assuming Newtonian gravity.

The g_2 -space geometries of the models and data from the SPARC database are classified and compared in a rescaled \hat{g}_2 -space that reduces systematic uncertainties on galaxy distance, inclination angle and variations in mass to light ratios.

We find that MOND modified inertia models, frequently used to fit rotation curve data, are disfavoured at more than 5σ independent of model details. The Bekenstein-Milgrom formulation of MOND modified gravity compares better with data in the analytic approximation we use. However a quantitative comparison with data is beyond the scope of the paper due to this approximation. NFW DM profiles only agree with a minority of galactic rotation curves.

Improved measurements of rotation curves, in particular at radii below the maximum of the total and the baryonic accelerations of the curves are very important in discriminating models aiming to explain the missing mass problem on galactic scales.

*Electronic address: frandsen@cp3.sdu.dk

†Electronic address: petersen@cp3.sdu.dk

I. INTRODUCTION

The fact that gravitational potentials on a range of astrophysical scales are deeper than predicted in Newtonian gravity is well established based on a variety of astronomical observations. These include measurements of the rotation curves of baryonic matter in galaxies [1–3], the velocity dispersion of galaxies in clusters [4], lensing of merging clusters [5] and measurements of the cosmic microwave background [6]. This fact is also referred to as the "missing mass problem" and observations on all the aforementioned scales have been argued to be in overall agreement with the presence of particle dark matter as the solution. Challenges for DM models in e.g. accounting for structure on small scales, such as the cusp-core problem [7], the missing satellites problem [8] and the too-big-to-fail problem [9] remain.

The observed rotation curves of baryonic matter in galaxies also motivates modified Newtonian dynamics (MOND) as an explanation for the problem [10]. In MOND the acceleration of test particles is modified, with respect to the Newtonian prediction, below a characteristic acceleration scale $a_0 \sim cH_0$, where c is the speed of light and H_0 the Hubble constant today. This modification accounts for the approximately flat asymptotic velocities of the galactic rotation curves at large radii [11–15] and the correlation of this asymptotic velocity with the total baryonic mass in the galaxy, i.e. the baryonic Tully-Fisher relation [16, 17]. On larger scales it has been found that MOND cannot account for the entire missing mass in galaxy clusters [18] or the dynamics of cluster mergers [19, 20]. Nor is it obvious if MOND can account for cosmological observations [21–23]. For a recent review of the observational status of MOND see [24].

Here we study galactic rotation curve data and the predicted curves in $(g_{\text{bar}}, g_{\text{tot}})$ -space (g -space) from MOND and DM models with $g_{\text{tot}}(r)$ being the total observed centripetal acceleration of matter in a rotationally supported galaxy as function of radial distance r from the center. Similarly $g_{\text{bar}}(r)$ is the centripetal acceleration arising from the baryonic (visible) matter distribution assuming Newtonian gravity.

We consider the predictions from two variants of MOND known as MOND modified inertia (MI) models [10, 25] which have been extensively employed to fit rotation curves [11–15, 26] and MOND modified gravity (MG) models in the Bekenstein-Milgrom formulation [27]. In the latter case we employ an analytic approximation for the predicted rotation curves [28]. For DM we consider the Navarro-Frenk-White [29] and the quasi-isothermal density profiles.

Rotation curve data from 175 galaxies in the SPARC database has recently been found to exhibit

the distinct $g2$ -space geometry of MOND modified inertia [13–15], termed the Mass Discrepancy Acceleration Relation (MDAR) [13, 30–32] and this has motivated the study of models that mimic this behaviour, both in DM e.g. [33–37] and in modified gravity frameworks [38–40]. It was however also found that ordinary Cold DM gives rise to this relation in the EAGLE simulation [41].

In this study we find that MOND modified inertia, independent of the specific model used, is disfavoured by the data at more than 5σ . More generally this holds for any model yielding a monotonically increasing function in $g2$ -space.

This paper is organized as follows:

In section II we illustrate different $g2$ -space geometries using a simple exponential disk model of the baryonic content of galaxies in Fig 1. We give a global classification of geometries using the relative locations of r_{bar} and r_{tot} — the radii of maximum baryonic and total accelerations respectively — summarized in table I. We then consider ratios of accelerations, $\hat{g}_{\text{bar}}(r) \equiv g_{\text{bar}}(r)/g_{\text{bar}}(r_{\text{bar}})$ and $\hat{g}_{\text{tot}}(r) \equiv g_{\text{tot}}(r)/g_{\text{tot}}(r_{\text{bar}})$ and illustrate the $\hat{g}2$ -space geometries in Fig. 2.

In section III we present our analysis of the SPARC rotation curve data [42] using the full inferred baryonic matter distribution, including disk, bulge and gas components. The data is shown in $g2$ -space and $\hat{g}2$ -space in Fig. 3. The latter eliminates systematic uncertainties on inclination angles and galaxy distances and reduces systematic uncertainties on mass-to-light ratios in the data.

We first show that the prediction $r_{\text{bar}} = r_{\text{tot}}$ from MOND modified inertia models, and consequently that $\hat{g}_{\text{bar,tot}}(r_{\text{bar}}) = \hat{g}_{\text{bar,tot}}(r_{\text{tot}})$, is in disagreement with data at more than 5σ . This is summarized in table II.

We next group the galaxies in SPARC according to the relative locations of r_{bar} and r_{tot} , summarized in table III and show the distribution of data in $\hat{g}2$ -space at radii above and below r_{bar} for the full SPARC data set and for each of these groups in Fig. 4. The average $\hat{g}2$ -space values of the full data set displays the characteristic geometry of DM with an isothermal density profile. This geometry is shared by the Bekenstein-Milgrom formulation of MOND modified gravity in the approximation used here. However the spread in data is significant. A minority of galaxies —which by selection have data only at large radii - display the characteristic geometry of MOND modified inertia on average while another minority displays that of DM with an NFW profile.

In section IV we summarize results and briefly discuss the limitations of our data analysis with respect to MOND modified gravity models and the relevance of improved measurements of rotation curves at small and moderate radii to probe the solution to the missing mass problem.

II. MODEL GEOMETRIES IN g_2 -SPACE

We begin by illustrating the geometry of MOND and DM models in g_2 -space in a simplified setting with the baryonic matter modelled purely as an infinitely thin disk with an exponential surface mass density

$$\Sigma(r) = \Sigma_0 e^{-r/r_d}, \quad (1)$$

where Σ_0 is the central surface mass density and r_d is the scale length. For all quantitative results later we instead use the inferred baryonic accelerations from the SPARC database [42]. We distinguish between two classes of MOND models that yield distinct geometries in g_2 -space, namely MOND modified inertia models (MI) [10, 25] — in which the Newtonian equation of motion is modified but Newtonian gravity is not — and MOND modified gravity models (MG) in the formulation of Bekenstein-Milgrom [27] in which the law of gravity itself is modified. Below we will refer to the total centripetal acceleration of a test mass in the midplane of a disk galaxy, of an unspecified model, as g_{tot} . The acceleration stemming from the visible matter assuming Newtonian gravity is termed g_{bar} . Finally when discussing specific models we will refer to the total acceleration with subscripts corresponding to that model, like g_{MI} for the total acceleration in a MOND modified inertia model.

MOND Models: In MOND modified inertia models the total centripetal acceleration, g_{MI} , on a test mass in the galactic plane is related to the Newtonian one, g_{bar} , via the relations

$$g_{\text{bar}}(g_{\text{MI}}) = \mu(x)g_{\text{MI}}, \quad x \equiv \frac{g_{\text{MI}}}{g_0}; \quad g_{\text{MI}}(g_{\text{bar}}) = \nu(y)g_{\text{bar}}, \quad y \equiv \frac{g_{\text{bar}}}{g_0}, \quad (2)$$

where $g_0 \sim 10^{-10} \frac{m}{s^2}$ is the characteristic acceleration scale of MOND. The interpolation function $\mu(x)$ smoothly interpolates between the deep Mondian regime $\mu(x) \simeq x$ for $x \ll 1$ and the Newtonian regime $\mu(x) \simeq 1$ for $x \gg 1$, but is otherwise undetermined at this level where a complete model of MOND modified inertia is not specified. The inverse interpolation function is $\nu(y) \equiv I^{-1}(y)/y$ with $I(x) = x\mu(x) = y$. Consequently in MOND modified inertia $g_{\text{MI}}(g_{\text{bar}})$ is a single valued function of g_{bar} .

In the Bekenstein-Milgrom formulation of MOND modified gravity models [27] the total centripetal acceleration is determined via a modified Poisson equation for the MOND potential field ψ

$$\vec{\nabla} \cdot \left(\mu \left(\frac{|\vec{\nabla}\psi|}{g_0} \right) \vec{\nabla}\psi \right) = 4\pi G\rho, \quad (3)$$

where the properties of the undetermined interpolation function is as above for MOND modified inertia. By noting that $4\pi G\rho = \vec{\nabla} \cdot \vec{g}_{\text{bar}}$, solutions to this equation are of the form

$$\vec{g}_{\text{bar}} = \mu\left(\frac{|\vec{\nabla}\psi|}{g_0}\right)\vec{\nabla}\psi + \vec{\nabla} \times \vec{h}, \quad (4)$$

where h is a generic vector field. An approximate expression for the resulting acceleration g_{MG} in MOND modified gravity, analogous to that in Eq. 2, for an exponential disk galaxy is derived in [28]:

$$g_{\text{bar}}(g_{\text{MG}}, r) = \mu\left(\frac{g_{\text{MG}}^+}{g_0}\right)g_{\text{MG}}, \quad g_{\text{MG}}(g_{\text{bar}}, r) = \nu\left(\frac{g_{\text{bar}}^+}{g_0}\right)g_{\text{bar}}; \quad (5)$$

$$g_{\text{MG}}^+ = I^{-1}(g_{\text{bar}}^+), \quad g_{\text{bar}}^+(g_{\text{bar}}, r) = \sqrt{g_{\text{bar}}^2 + (2\pi G\Sigma(r))^2}. \quad (6)$$

Due to the radial dependence of the fiducial quantities $g_{\text{bar},\text{MG}}^+$ the MOND modified gravity acceleration $g_{\text{MG}}(g_{\text{bar}}, r)$ is not a single valued function of the baryonic acceleration g_{bar} .

A number of interpolation functions $\mu(x)$ and inverse interpolation functions $\nu(y)$ have been considered in the literature, e.g. [43, 44]. For our analysis the details of the interpolation function are not central and we therefore focus on the inverse interpolation function from [24, 45] which was used to fit the SPARC galaxy data in [13, 14]:

$$\nu(y) = \frac{1}{1 - e^{-\sqrt{y}}}. \quad (7)$$

In order to classify $g2$ -space geometries and rotation curve data we define two reference radii, r_{bar} and r_{tot} as the radii at which g_{bar} and g_{tot} are maximum respectively,

$$g_{\text{bar}}(r_{\text{bar}}) = \max\{g_{\text{bar}}(r)\}, \quad g_{\text{tot}}(r_{\text{tot}}) = \max\{g_{\text{tot}}(r)\}. \quad (8)$$

We also define the curve segments \mathcal{C}^\pm above and below r_{bar} (similarly we could use r_{tot} as reference radius) of a given model in $g2$ -space as

$$\mathcal{C}^\pm = \{(g_{\text{bar}}(r), g_{\text{tot}}(r)); r \gtrless r_{\text{bar}}\}. \quad (9)$$

In the left panel of Fig. 1 we show the MOND modified inertia curve from Eq. (2) (solid line) and the approximate modified gravity curve from Eq. (6) (dotted and dashed curves). The reference radii $r_{\text{bar,obs}}$ are indicated with dots while the grey curve segments correspond to \mathcal{C}^+ and the black curve segments to \mathcal{C}^- .

In MOND modified inertia models $r_{\text{bar}} = r_{\text{tot}}$ and the two curve segments coincide, ie. $\mathcal{C}^- = \mathcal{C}^+$, as consequences of the MOND modified inertia function $g_{\text{MI}}(g_{\text{bar}})$ being single valued. Equivalently, the area enclosed by the MOND modified inertia curve \mathcal{C}_{MI} is zero, $\mathcal{A}(\mathcal{C}_{\text{MI}}) = 0$ as discussed in [46].

In the MOND modified gravity approximation of Eq. (6) it follows that $r_{\text{bar}} < r_{\text{tot}}$ and the curve segment \mathcal{C}^+ is above the curve segment \mathcal{C}^- in $g2$ -space. Equivalently, the enclosed area of the MOND modified gravity curve is non-zero $\mathcal{A}(C_{\text{MG}}) > 0$. We summarize these properties in the first two rows of table I.

In Fig. 1 we have used the exponential disk in Eq. (1) for the baryonic matter distribution, for which $r_{\text{bar}} \simeq 0.41r_d$ and the interpolation function corresponding to Eq. (7). Since $g_{\text{bar}}(r = 0) = g_{\text{bar}}(r = \infty) = 0$ the curves shown are closed with curve parameters $0 \leq r \leq \infty$. The scale length r_d of the exponential disk does not influence the geometry of the curves but only how much of the curve is traced up to a given radius r . The central surface density Σ_0 scales the maximum values of g_{bar} , and g_{tot} and therefore stretches or shrinks the curves. For MOND modified inertia, curves with smaller Σ_0 coincide with a part of those with a larger Σ_0 . For MOND modified gravity we illustrate the shrinking and stretching by plotting two different values of Σ_0^{-1} . In both cases, for a given interpolation function and acceleration scale g_0 , the $g2$ -space curves are completely determined for all galaxies by the baryonic matter distribution. .

Dark Matter: In DM models the total centripetal acceleration $g_{\text{DM}}(r) = g_{\text{bar}}(r) + g_{\text{halo}}(r)$ is a sum of the contributions from the baryonic and DM density distributions — here assumed to be a spherical halo for simplicity. To illustrate the $g2$ -space geometry of the considered dark matter models we again employ the exponential disk in Eq.(1) for the baryonic matter and two different DM density profiles

$$\rho_{\text{NFW}}(r) = \frac{\rho_{0,\text{NFW}}}{\frac{r}{r_s} \left(1 + \frac{r}{r_s}\right)^2}, \quad \rho_{\text{ISO}}(r) = \frac{\rho_{0,\text{ISO}}}{1 + \left(\frac{r}{r_c}\right)^2}, \quad (10)$$

where $\rho_{0,\text{NFW}}, \rho_{0,\text{ISO}}$ are mass densities and r_s, r_c are scale lengths respectively. The Navarro-Frenk-White profile $\rho_{\text{NFW}}(r)$ is motivated by fits to the density of halos in simulations of cold collisionless DM [47] and leads to a cuspy central DM density profile at small radii scaling as $\rho_{\text{NFW}}(r) \sim r^{-1}$. The quasi-isothermal DM density profile $\rho_{\text{ISO}}(r)$ may be physically realized (at small radii) in models with sizeable DM self interactions and leads to a cored DM density profile at small radii scaling as $\rho_{\text{ISO}}(r) \sim r^0$. It has recently been proposed that the diversity of galactic rotation curves [48] can be accommodated in a model of self interacting DM where the resulting DM density profile is approximately quasi-isothermal profile at small radii, set by the DM density and self-interaction cross-section, while following the NFW profile at large radii [49, 50]. For both density profiles the

¹ If the galactic mass is kept fixed r_d and Σ_0 cannot be varied independently

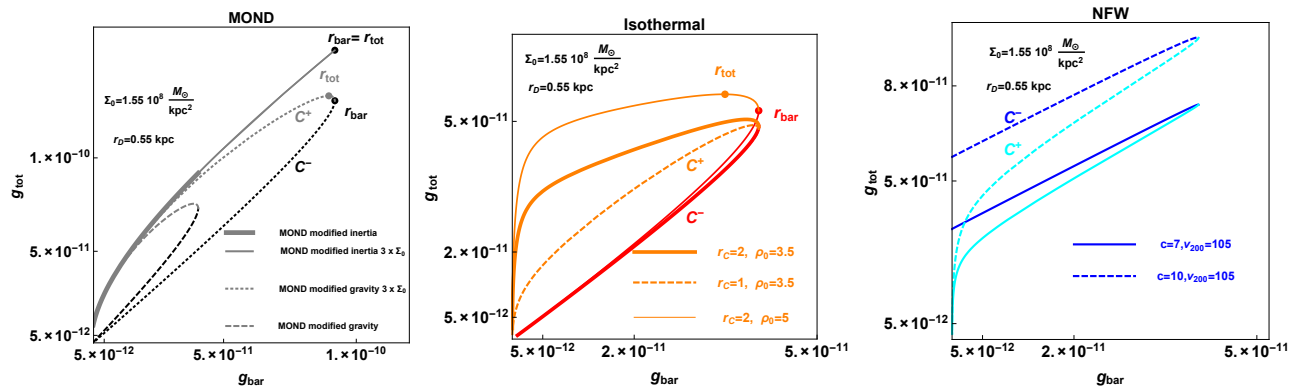


FIG. 1: The g_2 -space geometry of MOND and DM models using texponential disk in Eq. 1 for the baryonic matter with scale height $r_D = 0.55$ kpc.

Left Panel: MOND modified inertia (solid thick and thin) curves and MOND modified gravity (dotted and dashed curves) with interpolation function in Eq. (7), and for MOND modified gravity, the approximation in Eq. (6). We show two values of the central surface density $\Sigma_0 = 1.55 \times 10^8 M_\odot/\text{kpc}^2$ (solid thin and dotted) and $3 \times \Sigma_0$ (solid thick and dashed). The reference radii r_{bar} and r_{tot} defined in Eq. 8 and the curve segments \mathcal{C}^\pm as defined in Eq. 9 are shown for two of the curves.

Middle panel: DM models with quasi-isothermal density profiles for different values of the DM density scale radius r_c and central density ρ_0 .

Right Panel: DM models with NFW density profiles for different values of velocity v_{200} at the virial radius r_{200} and the concentration parameter $c = r_{200}/r_s$ and v_{200} .

centripetal accelerations in the midplane of a disk galaxy $g_{\text{NFW}}(g_{\text{bar}}, r)$, $g_{\text{ISO}}(g_{\text{bar}}, r)$ are not single valued functions of g_{bar} .

We show examples of DM model curves in g_2 -space for the quasi-isothermal and NFW profiles respectively in the middle and right panels of Fig. 1. The curve segments \mathcal{C}^+ are shown in orange and cyan respectively while the curve segments \mathcal{C}^- are shown in red and blue respectively. The full curves in the quasi-isothermal case are closed curves, since also $g_{\text{ISO}}(r = 0) = g_{\text{ISO}}(\infty) = 0$ while the area of the curve is non-zero $\mathcal{A}(C_{\text{ISO}}) > 0$ as discussed in [46]. The width of the curve is controlled by ρ_0 , as seen by comparing the solid thick and solid thin curves, while the steepness of the curve near $r = 0$ is controlled by r_c as seen by comparing the dashed and dotted curves. .

The NFW curves are distinct by not being closed due to the divergence of the profile at small r — the cuspyness of the NFW profile translates into $g_{\text{tot,DM}}(r = 0) > 0$ — and by the fact that the curve segments \mathcal{C}^+ lie below the curve segments \mathcal{C}^- . The width of the NFW curve is controlled by

Models	Reference radii	Curve segments	Curve Area ^a
MOND-MI	$r_{\text{tot}} = r_{\text{bar}}$	$\mathcal{C}^+ = \mathcal{C}^-$	$\mathcal{A}(\mathcal{C}) = 0$
MOND-MG	$r_{\text{tot}} > r_{\text{bar}}$	$\mathcal{C}^+ > \mathcal{C}^-$	$\mathcal{A}(\mathcal{C}) > 0$
DM-ISO	$r_{\text{tot}} > r_{\text{bar}}$	$\mathcal{C}^+ > \mathcal{C}^-$	$\mathcal{A}(\mathcal{C}) > 0$
DM-NFW	$r_{\text{tot}} < r_{\text{bar}}$	$\mathcal{C}^+ < \mathcal{C}^-$	Curves open

^aThe curves are closed and the areas spanned by the curves, $\mathcal{A}(\mathcal{C})$, are defined for the first three models provided the baryonic accelerations satisfy $g_{\text{bar}}(r=0) = g_{\text{bar}}(r=\infty) = 0$ as is the case for an exponential disk.

TABLE I: Global characteristics of geometries in $g2$ -space for MOND and DM models as shown in Fig. 1. The reference radii r_{tot} and r_{bar} are the radii of maximum total acceleration and maximum inferred baryonic acceleration, as defined in Eq. (8) and the curve segments \mathcal{C}^\pm are defined in Eq. (9).

the concentration parameter $c = \frac{r_{\text{vir}}}{r_s}$, where r_{vir} is the virial radius, as seen by comparing the solid and dashed curves.

We summarize the characteristics of the model geometries in Table I. For MOND modified inertia models $r_{\text{tot}} = r_{\text{bar}}$ and $\mathcal{C}^- = \mathcal{C}^+$ and consequently $\mathcal{A}(\mathcal{C}_{\text{MI}}) = 0$. For MOND modified gravity and quasi-isothermal DM models $r_{\text{tot}} > r_{\text{bar}}$ and the curve segments \mathcal{C}^+ lie above \mathcal{C}^- in g_{tot} values and consequently $\mathcal{A}(\mathcal{C}_{\text{ISO}}) > 0$. Finally for NFW DM models the curve segments \mathcal{C}^- lie above \mathcal{C}^+ in g_{tot} (with $r_{\text{tot}} < r_{\text{bar}}$ barely visible) and the area is undefined. The degeneracy of the MOND modified gravity approximation and DM-ISO geometries with respect to these basic characteristics, does not imply the geometry is identical as is evident from Fig. 1. In particular the shape of the DM-ISO curves is controlled by the scale length of the DM density an additional free parameter as compared to the MOND modified gravity approximation.

Normalized $\hat{g}2$ -space: In order to display the average geometry of several galactic rotation curves and to reduce systematic uncertainties it is relevant to consider ratios of accelerations in a normalized $\hat{g}2$ -space by defining

$$\hat{g}_{\text{bar,tot}}(r) \equiv g_{\text{bar,tot}}(r)/g_{\text{bar,tot}}(r_{\text{bar}}). \quad (11)$$

Another possibility here would be to use r_{tot} as a reference radii in the denominator above. We replot the MOND and DM model geometries from Fig. 1 in the rescaled $\hat{g}2$ -space in Fig (2).

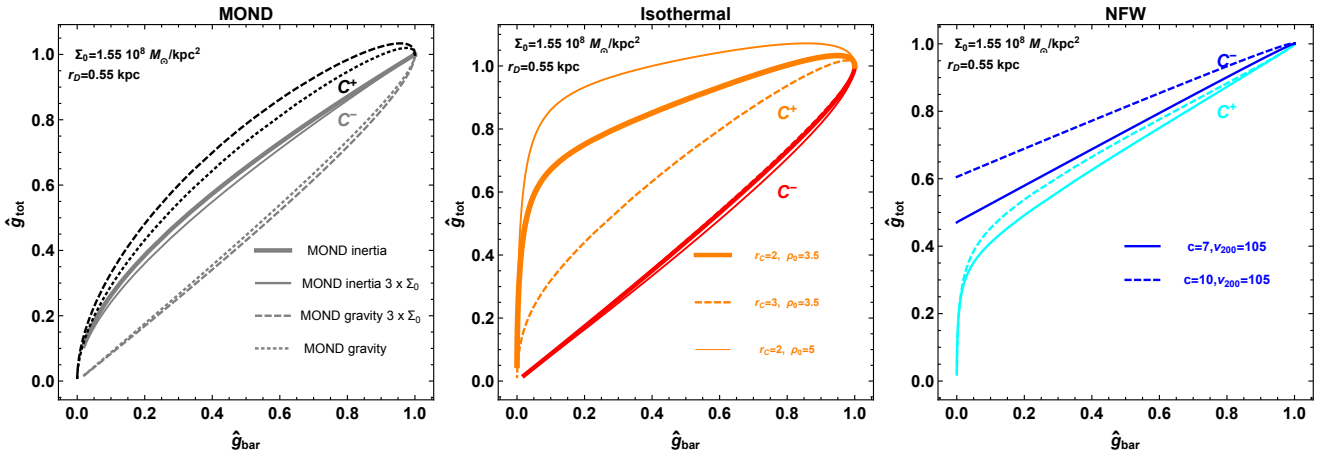


FIG. 2: The $\hat{g}2$ -space geometry ($\hat{g}_{\text{bar}}(r), \hat{g}_{\text{tot}}(r)$) of MOND and DM models as defined in Eq. (11). Curves and parameters are otherwise identical to those in Fig. 1.

III. DATA ANALYSIS

We study rotation curve data from the 175 galaxies in the SPARC database [42]. The database provides the observed total rotational velocities $v_{\text{obs}}(r_j)$, as a function of observed radii points r_j . The database also provides the inferred rotational velocities $v_{\text{disk}}(r_j)$, $v_{\text{bul}}(r_j)$, $v_{\text{gas}}(r_j)$ from the baryonic matter components of the galaxies, divided into stellar disks, bulges and gas components. From this we compute the inferred baryonic acceleration $g_{\text{bar}}(r_j)$, and the total observed acceleration $g_{\text{obs}}(r_j)$ at each radii r_j as

$$g_{\text{obs}}(r_j) = \frac{v_{\text{obs}}^2(r_j)}{r_j}, \quad g_{\text{bar}}(r_j) = \frac{(v_{\text{gas}}^2(r_j) + \Upsilon_{\text{disk}} v_{\text{disk}}^2(r_j) + \Upsilon_{\text{bul}} v_{\text{bul}}^2(r_j))}{r_j}. \quad (12)$$

We adopt as central values for the mass to light ratios $\Upsilon_{\text{disk}} = 0.5 \frac{M_{\odot}}{L_{\odot}}$ and $\Upsilon_{\text{bulge}} = 0.7 \frac{M_{\odot}}{L_{\odot}}$. The SPARC data base also provides the corresponding (random) uncertainties $\delta v_{\text{obs}}(r_j)$, as well as the uncertainties δi and δD on the galaxy inclination angle i and distance D . Following [42] we further adopt a 10 percent uncertainty on v_{gas} and 25 percent uncertainties on $\Upsilon_{\text{disk,bulge}}$, i.e. $\delta v_{\text{gas}} = 0.1 v_{\text{gas}}$ and $\delta \Upsilon_{\text{disk,bulge}} = 0.25 \Upsilon_{\text{disk,bulge}}$. With this input we compute the $\delta g_{\text{bar}}, \delta g_{\text{obs}}$ uncertainties

$$\delta g_{\text{obs}}(r_j) = g_{\text{obs}}(r_j) \sqrt{\left[\frac{2\delta v_{\text{obs}}(r_j)}{v_{\text{obs}}(r_j)} \right]^2 + \left[\frac{2\delta i}{\tan(i)} \right]^2 + \left[\frac{\delta D}{D} \right]^2}, \quad (13)$$

$$\delta g_{\text{bar}}(r_j) = \frac{\sqrt{(2v_{\text{gas}}(r_j))^2 \delta v_{\text{gas}}^2 + v_{\text{disk}}^4(r_j) \delta \Upsilon_{\text{disk}}^2 + v_{\text{bulge}}^4(r_j) \delta \Upsilon_{\text{bulge}}^2}}{r_j}.$$

where we note that the inferred $g_{\text{bar}}(r_j)$ are independent of distance D and inclination angle i [15].

We treat the uncertainties $\delta v_{\text{obs}}, \delta v_{\text{gas}}$ as random gaussian errors for each data point while the remaining uncertainties, $\delta i, \delta D, \delta \Upsilon_{\text{disk,bulge}}$ are systematic errors, rescaling all data points within a galaxy in the same direction. To reduce these systematic uncertainties we will analyze ratios of accelerations as in Eq. (11), defining:

$$\hat{g}(r_j)_{\text{bar,obs}} = \frac{g(r_j)_{\text{bar,obs}}}{g(r_{\text{bar}})_{\text{bar,obs}}}, \quad \hat{g}(\Delta r)_{\text{bar,obs}} = \frac{g(\Delta r)_{\text{bar,obs}}}{g(\Delta r_{\text{bar}})_{\text{bar,obs}}}; \quad g(\Delta r)_{\text{bar,obs}} \equiv \frac{1}{N_{\Delta}} \sum_{j \in \Delta r} g(r_j)_{\text{bar,obs}} \quad (14)$$

where Δr denotes an interval centered on r that we average g over within a galaxy, Δr_{bar} is an equivalent interval around r_{bar} and N_{Δ} denote the number of points in the interval.

The ratios $\hat{g}_{\text{obs}}(r_j)$ and $\hat{g}_{\text{obs}}(\Delta r)$ eliminate the systematic uncertainties $\delta i, \delta D$ in galaxy inclination angle i and galaxy distance D , up to any significant variation of inclination angle with radius within a single galaxy [15], while $\hat{g}_{\text{obs}}(\Delta r)$, reduces the systematic error introduced by the single normalization point $g_{\text{obs}}(r_{\text{bar}})$ in $\hat{g}_{\text{obs}}(r_j)$ when averaging over several galaxies. As we show explicitly in the appendix $\hat{g}_{\text{bar}}(r_j)$ and $\hat{g}_{\text{bar}}(\Delta r)$ reduce the systematic uncertainties in $\delta \Upsilon_i$ significantly, especially near r_{bar} by construction, where we are particularly interested in the geometry. These three sources of systematic uncertainties were found to be the dominant sources of scatter in previous analysis [15]. With the above construction there is only a small remaining systematic error on $\hat{g}_{\text{bar}}(r_j)$ from mass to light ratios contained in the small quantity $\Delta \Upsilon$, in Eq. (A5). This means we can to a good approximation take the errors of $\hat{g}_{\text{obs,bar}}(r_j)$ and $\hat{g}_{\text{obs,bar}}(\Delta r)$ from different galaxies to be uncorrelated, even if the error on the mass to light ratios should be correlated for different galaxies. There is also a possible systematic uncertainty on $\hat{g}_{\text{obs}}(\Delta r)$ from data points which may be included in both numerator and denominator when Δr and Δr_{bar} overlap. This part of the error budget for $\hat{g}_{\text{obs}}(\Delta r)$ is however completely uncorrelated between different galaxies under the assumption that v_{obs} values are uncorrelated. The details of the errors are discussed in the appendix A.

A. Data Selection

We begin with the 175 galaxies in the SPARC database and discard 22 galaxies based on the same quality criteria applied in [13, 14]. Ten of these are face-on galaxies with inclination angle $i < 30^\circ$ that are rejected to minimize corrections to the observed velocities and twelve are galaxies with asymmetric rotation curves that do not trace the equilibrium gravitational potential. We discard one more galaxy, UGC01281, with large negative inferred speeds v_{gas} for the gas component leaving

152 galaxies with 3143 data points. A further data requirement $\delta v_{\text{obs}}/v_{\text{obs}} < 0.1$ was imposed in [13, 14]. We only include this additional requirement when explicitly stated, e.g in the data sample N_{G_2} discussed below, and otherwise keep all the 3143 data points.

We show (a part of) the collection of SPARC data in g_2 -space from these 152 galaxies in the top left panel of Fig. 3 (gray dots) across 3 orders of magnitude in g_{bar} . Also shown in the figure panel are the curves of individual galaxies with error bars that were highlighted in [46]. These error bars include both random and systematic errors from Eq. 14. The blue line is the MOND modified inertia function in Eq. (7) with $g_0 \simeq 1.2 \times 10^{-10} \frac{m}{s^2}$. This value of g_0 is the best fit value to the entire data set found in [13, 14] with the additional data requirement of $\delta v_{\text{obs}}/v_{\text{obs}} < 0.1$. The top right panel shows the same figure with this requirement $\delta v_{\text{obs}}/v_{\text{obs}} < 0.1$ imposed. Finally the bottom panels show the same data in the normalized \hat{g}_2 -space.

While the entire collection of data traces the MOND modified inertia curve, as observed and quantified in [13, 14], it also appears that individual galaxies deviate significantly from this curve.

In order to test the geometry of the data we therefore first consider 3 subsets of data points from the 152 galaxies, $N_{1,2,3}$. We denote the set of 152 data points with radii $r_j = r_{\text{obs}}$ by N_1 and the remaining 146 data points after first requiring $\delta v_{\text{obs}}/v_{\text{obs}} < 0.1$ as in [13, 14] by N_2 . Computing the averages $\langle \hat{g}_{\text{obs,bar}} \rangle$ on these sets we find that the N_1 and N_2 data sets yield 3σ and more than 5σ discrepancy respectively with the MOND modified inertia prediction $\langle \hat{g}_{\text{obs}}(r_{\text{obs}}) \rangle_{\text{MI}=1}$. The discrepancies with the prediction $\langle \hat{g}_{\text{bar}}(r_{\text{obs}}) \rangle_{\text{MI}=1}$ are larger as summarized in table II. To improve

Data Sets	Galaxies	Data selection	Data points	$\langle \hat{g}_{\text{obs}} \pm \delta \hat{g}_{\text{obs}} \rangle$	$\langle \hat{g}_{\text{bar}} \pm \delta \hat{g}_{\text{bar}} \rangle$
N_1	152	$r_j = r_{\text{obs}}$	152	1.39 ± 0.12	0.83 ± 0.01
N_2	152	$r_j = r_{\text{obs}}$ and $\delta v_{\text{obs}}/v_{\text{obs}} < 0.1$	146	1.12 ± 0.02	0.91 ± 0.01
N_3	152	$r_{\text{obs,bar}+1} \geq r_j \geq r_{\text{obs,bar}-1}$	$\sim 400^a$	1.23 ± 0.04	0.89 ± 0.01

^a402 points with $r_{\text{obs}+1} \geq r_j \geq r_{\text{obs}-1}$ and 393 with $r_{\text{bar}+1} \geq r_j \geq r_{\text{bar}-1}$ where in some cases there is e.g. no data point at radii below r_{bar} .

TABLE II: Data sets $N_{1,2}$ on which the averages $\langle \hat{g}_{\text{obs,bar}}(r_{\text{obs}}) \rangle$ and errors are computed and N_3 on which $\langle \hat{g}_{\text{obs,bar}}(\Delta r_{\text{obs}}) \rangle$ is computed. The MOND modified inertia predictions are $\langle \hat{g}_{\text{obs,bar}}(r_{\text{obs}}) \rangle_{\text{MI}=1} = \langle \hat{g}_{\text{obs,bar}}(\Delta r_{\text{obs}}) \rangle_{\text{MI}} = 1$.

the significance we consider a larger data set N_3 with a range $r_j \in \Delta r_{\text{obs,bar}}$ of points around $r_{\text{obs,bar}}$

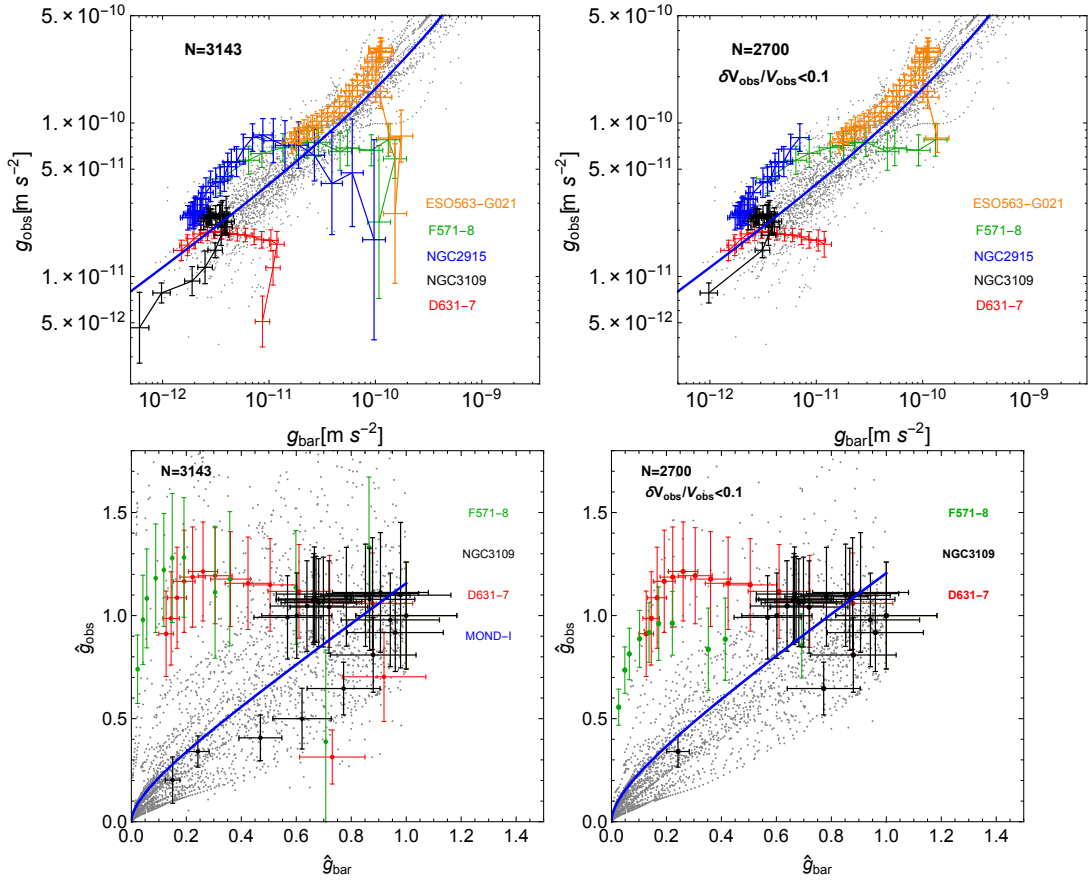


FIG. 3: SPARC data in g_2 -space (upper panels) and \hat{g}_2 -space (lower panels). The full sets of data points without errors are shown as gray dots (3143 points on left panels) and also when imposing $\delta v_{\text{obs}}/v_{\text{obs}} < 0.1$ (2700 points on right panels). On all panels we also show the prediction from MOND modified inertia with $g_0 = 1.2 \times 10^{-10} \frac{\text{m}}{\text{s}^2}$ (blue) and individual galaxies with associated errors from Eq. (14) are highlighted (color legend on figure). On the lower panels fewer individual galaxies are displayed for visual clarity.

defined here via $r_{\text{obs,bar}} + 1 \geq r_j \geq r_{\text{obs,bar}} - 1$. We compute $\hat{g}_{\text{obs}}(\Delta r_{\text{obs}})$ as defined above using these points for each galaxy and finally the galaxy averages $\langle \hat{g}_{\text{obs,bar}}(\Delta r_{\text{obs}}) \rangle$ over all galaxies with this data. Here we find more than 5σ discrepancy from the MOND modified inertia prediction of unity with both the $\hat{g}_{\text{obs,bar}}$ observables. The results are summarized in the last row in Table II.

The numbers summarized in Table II imply that MOND modified inertia does not correctly describe the SPARC data, even if the overall scatter around the fitting function (7) was found to be small in [13, 14]. To study the geometry of the SPARC data further we group the entire data set into points N_G^+ at $r \geq r_{\text{bar}}$ and points N_G^- at $r < r_{\text{bar}}$. We further divide the galaxies into 3 groups $G_{1,2,3}$, motivated by the theoretical characterization in Table I. Galaxies in G_1 satisfy $r_{\text{bar}} = r_{\text{tot}}$,

galaxies in G_2 satisfy $r_{\text{bar}} < r_{\text{tot}}$, and galaxies in G_3 satisfy $r_{\text{bar}} > r_{\text{tot}}$. The set of data points in G_1 is N_{G_1} while we divide each set of data points within $G_{1,2}$ into subsets $N_{G_2}^+$, $N_{G_3}^+$ with $r_j > r_{\text{bar}}$ and $N_{G_2}^-$ and $N_{G_3}^-$ with $r_j < r_{\text{bar}}$. We summarize the datasets in table III below. Within the above 7

Data set	Galaxy selection	Data selection	Data points
N_G^+	all (152)	$r_j > r_{\text{bar}}$	2695
N_G^-	all (152)	$r_j \leq r_{\text{bar}}$	296
N_{G_1}	$r_{\text{obs}} = r_{\text{bar}}$ (29)	all	933
$N_{G_2}^+$	$r_{\text{obs}} > r_{\text{bar}}$ (86)	$r_j > r_{\text{bar}}$	1179
$N_{G_2}^-$	$r_{\text{obs}} > r_{\text{bar}}$ (86)	$r_j \leq r_{\text{bar}}$	140
$N_{G_3}^+$	$r_{\text{obs}} < r_{\text{bar}}$ (37)	$r_j > r_{\text{bar}}$	764
$N_{G_3}^-$	$r_{\text{obs}} < r_{\text{bar}}$ (37)	$r_j \leq r_{\text{bar}}$	127

TABLE III: Summary of galaxy group and corresponding data points used in Fig. 4 to show the average geometry of data.

galaxy data groups $N_G^\pm, N_{G_1}, N_{G_{2,3}}^\pm$ we bin the normalized baryonic accelerations $\hat{g}_{\text{bar}}(r_j)$ in 4 bins of width $\hat{g}_{\text{bar},k} - \hat{g}_{\text{bar},k-1} = \Delta\hat{g}_{\text{bar}} = 0.25$ with $k = 1, \dots, 4$ and compute the average values $\langle \hat{g}_{\text{bar,obs}} \rangle_{N_{G_i,k}^\pm}$ and associated errors $\delta \langle \hat{g}_{\text{bar,obs}} \rangle_{N_{G_i,k}^\pm}$ discussed in the appendix.

We show the data groups $N_G^\pm, N_{G_1}, N_{G_{2,3}}^\pm$ together with the binned averages of each corresponding data set in Fig. 4. On all 4 panels the solid black line is the MOND modified inertia prediction while the solid and dashed gray lines are the predictions from the Bekenstein-Milgrom MOND modified gravity approximation at radii above and below r_{bar} . We keep the discussion below qualitative as we have already presented the quantitative discrepancy with MOND modified inertia and because our treatment of MOND modified gravity relies on the approximation for purely disk galaxies in [28].

The top left panel shows data from the full group of SPARC galaxies, equivalent to Fig 3, but with data divided into the two groups N_G^\pm . The data (light purple and purple dots) is seen to display the geometry characterized by $r_{\text{tot}} > r_{\text{bar}}$ in table I on average. MOND modified inertia (black line) is a good description of the average values of N_G^+ (light purple points with errors) but not in N_G^- (purple points with errors) at large accelerations. Also the panel shows a large overall spread in data in \hat{g} -space compared to the data errors on the averages. MOND modified gravity

(solid gray for $r \geq r_{\text{bar}}$ and dashed gray line for $r < r_{\text{bar}}$) is a better description of data except for points at $r < r_{\text{bar}}$ with small accelerations. The panel also shows a large overall spread in data in \hat{g}^2 -space compared to the data errors on the averages.

The top right panel displays the same quantities but for the data set N_{G_1} where galaxies have $r_{\text{tot}} = r_{\text{bar}}$. Here MOND modified inertia is a very good description of the averaged data — which by selection only samples radii $r \geq r_{\text{bar}}$. Both the average measurement error and the spread in data is smaller than for the full data set (both at $r < r_{\text{bar}}$ and at $r \geq r_{\text{bar}}$) on the left panel.

The bottom left panel is for the $N_{G_2}^+$ and $N_{G_2}^-$ data sets with $r_{\text{tot}} > r_{\text{bar}}$ which is true for most of the galaxies (86) and these galaxies are driving the overall geometry and data spread seen in the top left panel. Despite this spread and the greater average errors there is a clear difference between the two data sets $N_{G_2}^+$ and $N_{G_2}^-$ with MOND modified inertia a poor description of $N_{G_2}^-$ data. Again the MOND modified gravity prediction is clearly a better match to the data, but as opposed to the full data set in the top left panel, it is now the data at $r < r_{\text{bar}}$ and large accelerations that yields the biggest deviations.

Finally the right hand panel shows the results for the $N_{G_3}^+$ and $N_{G_3}^-$ data sets with $r_{\text{tot}} < r_{\text{bar}}$. Here only the spread and errors of the $N_{G_3}^-$ set is big as compared to the N_2 set, with MOND modified inertia model match to the average values of both data sets. Inevitably the MOND modified gravity approximation is also a poor match to the average values of the $N_{G_3}^-$ as the MOND modified gravity approximation always leads to $r_{\text{tot}} > r_{\text{bar}}$

Again we do not here quantify the deviations of the MOND modified gravity approximation, as this approximation was developed for an infinitely thin disk galaxy geometry [28] and also does not take into account the external field effect [51] in MOND modified gravity, which might be important for some non-isolated galaxies, see e.g. the recent discussion of the 'dark matter less' dwarf galaxy NGC-1052-DF2 and MOND [52, 53]. The analysis does show that the disagreement is driven by the majority of galaxies exhibiting geometries with $r_{\text{tot}} > r_{\text{bar}}$ but it is offset by a minority of galaxies exhibiting $r_{\text{tot}} < r_{\text{bar}}$. This, together with the fact that most data is measured at $r > r_{\text{bar}}$, means that as a whole the SPARC rotation curve data exhibits moderate and Gaussian residuals around the function (7) as found in [13]. This however does not reflect the average geometry of the rotation curves. Our analysis therefore highlights the need to further study MOND Modified gravity models, beyond the MOND modified inertia models most often used in the literature, in order to establish if MOND can account for rotation curve data.

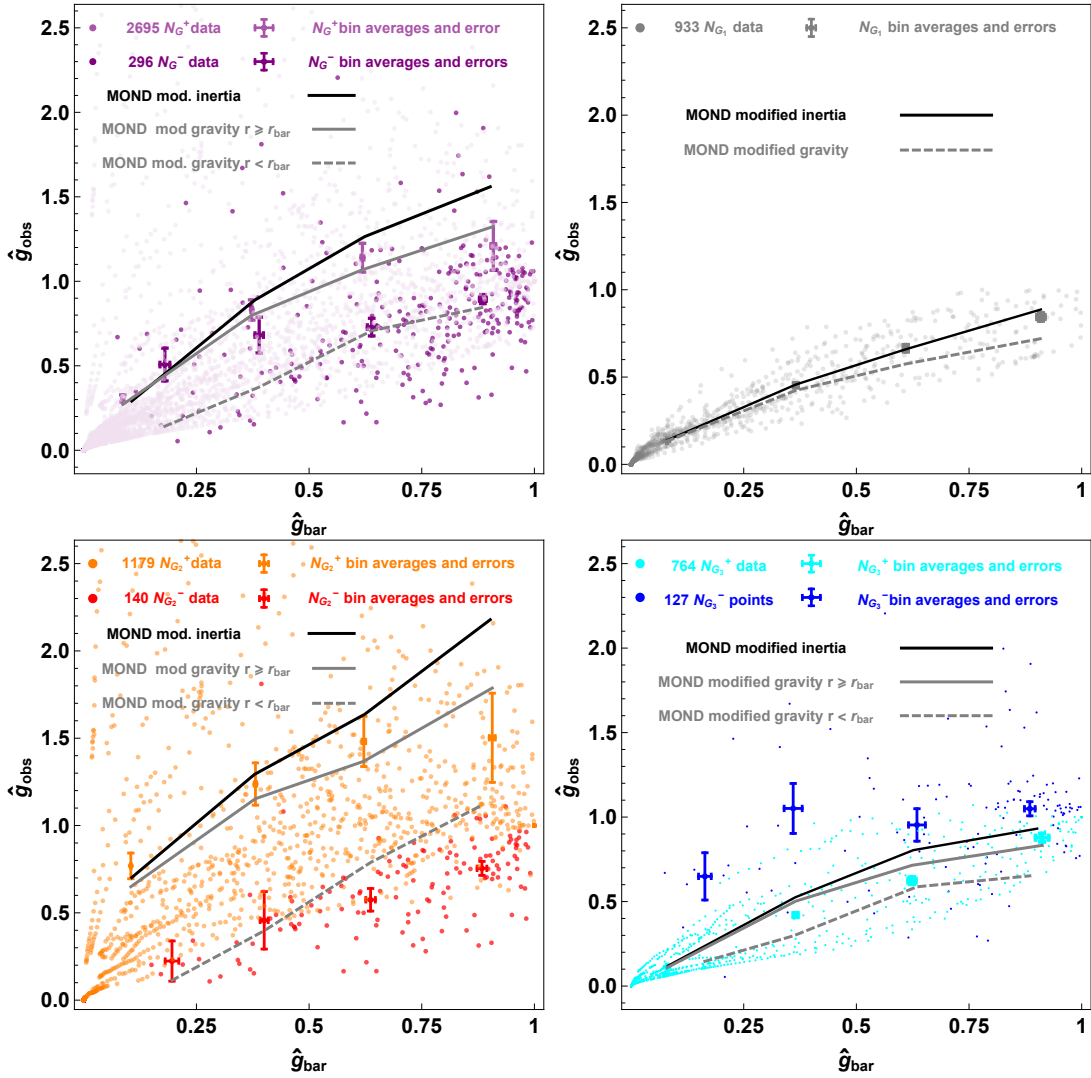


FIG. 4: SPARC rotation curve data and data averages with errors in the normalized $\hat{g}2$ -space.

Top left panel: The full SPARC data set (shown without errors) divided into points in N_G^+ with $r > r_{\text{bar}}$ (light purple) and those in N_G^- with $r < r_{\text{bar}}$ (purple). Also shown are the average data values and their errors computed within the 4 \hat{g}_{bar} bins in N_G^\pm (light purple and purple error bars) as discussed in the text. Finally we show the averaged prediction from MOND MI (black curve) and MOND MG for $r > r_{\text{bar}}$ (gray solid) and for $r < r_{\text{bar}}$ (gray dashed).

Top right panel: The same as top left but for all data in N_{G_1} (galaxies where $r_{\text{obs}} = r_{\text{bar}}$) without distinguishing between $r > r_{\text{bar}}$ or $r < r_{\text{bar}}$.

Bottom left panel: The same as top left but for data in N_{G_2} (galaxies where $r_{\text{obs}} > r_{\text{bar}}$).

Bottom right panel: The same as top left but for data in N_{G_3} (galaxies where $r_{\text{obs}} < r_{\text{bar}}$).

IV. SUMMARY

We have shown the g_2 -space geometry of selected MOND and DM models for disk galaxies with exponential mass densities for the visible baryonic mass distribution in Fig. 1 — these are MOND modified inertia and an approximate description of Bekenstein-Milgrom MOND modified gravity models as well as DM models with NFW and quasi-isothermal DM density profiles.

We have classified the g_2 -space geometry of these models in Figs. 1 and 2 using global characteristics: The location of the maximum acceleration due to the baryonic matter and the maximum of the total predicted acceleration, r_{bar} and r_{tot} , whether the curve is closed or open and the area of the closed curves $\mathcal{A}(\mathcal{C})$. MOND modified inertia models, DM models with NFW profiles and DM models with quasi-isothermal profiles can be organized in distinct categories according to these global characteristics, while MOND modified gravity models in the approximation used is degenerate with DM models with quasi-isothermal profiles as summarized in table I.

Rotation curve data may also be organized according to this classification. Applying this classification to rotation curve data from the SPARC data base we find that MOND modified inertia, independent of the specific interpolation function used, is in disagreement with the data at more than 5σ . A previous analysis finding disagreement between MOND modified inertia and SPARC data was presented in [46]. In the current analysis we have considered ratios of accelerations $\hat{g}_{\text{bar,obs}}(r) \equiv g_{\text{bar,obs}}(r)/g_{\text{bar,obs}}(r_{\text{bar}})$ with respect to some reference acceleration, here chosen as $g(r_{\text{bar}})$ in order to reduce the systematic uncertainties in data stemming from galaxy inclination angles i and distances D on g_{obs} as well as mass to light ratios $\Upsilon_{\text{disk,bulge}}$ on g_{bar} . If there is a strong radial dependence of these quantities within individual galaxies, and/or between galaxies this can still affect our results. However, changing the conclusion that MOND modified inertia models do not fit the data would require significant radius variations from r_{bar} to r_{tot} . A detailed study of this is beyond the scope of this paper, but e.g. a monotonically decreasing dependence of mass to light ratios with radius [54, 55] will not change our result that MOND modified inertia is not in agreement with data.

We have presented the rotation curve data from the SPARC data base organized according to the relative location of $r_{\text{bar,tot}}$ in \hat{g}_2 -space in table III and Fig. 4. In addition to the quantitative results on MOND modified inertia, these figures establish qualitatively that subsets of galaxies display different geometric characteristics and neither MOND modified inertia nor MOND modified gravity describe all data subsets. If all data is joined together a fit to MOND modified inertia with

gaussian errors and moderate scatter can be obtained [13] since the average data from the data sets $N_{G_2}^-$ and $N_{G_3}^-$ deviate in opposite directions from the MOND modified inertia prediction and since most data points are measured at $r > r_{\text{bar}}$ where deviations from MOND modified inertia are not as significant. Since the global geometrical characteristics of the other considered models, both MOND modified gravity (in the approximation employed), DM with isothermal density profile and DM with NFW density profile, differ from MOND modified inertia exactly for data points at $r < r_{\text{bar}}$ it is important to investigate these separately.

In summary we find that MOND modified inertia models, frequently used to fit rotation curve data, are not in agreement with data, while further study of MOND modified gravity models would be required to establish those as a viable explanation of data. Further we find that the detailed geometry in g_2 -space is useful to probe different DM density distributions, with e.g. only a minority of galaxies exhibiting the global characteristics of NFW profiles. This latter conclusion is well known in the guise of the cusp-core problem. However the g_2 -space analysis makes it apparent how in particular future improvements in rotation curve data at small radii is extremely useful in probing the DM density profile. This may yield new insights on the required particle physics characteristics of DM, e.g. DM self interactions. More generally the g_2 -space analysis offers a very useful and striking characterization of models for the missing mass problem.

Acknowledgments: We thank W-C. Huang and I. Shoemaker for comments on the draft. The authors acknowledge partial funding from The Council For Independent Research, grant number DFF 6108-00623. The CP3-Origins center is partially funded by the Danish National Research Foundation, grant number DNRF90.

Appendix A: Error treatment

In this appendix we review calculation of errors used throughout the paper. The errors $\delta g_{\text{obs,bar}}(r_j)$ on individual $g_{\text{obs,bar}}(r_j)$ points are given in the main text in Eq. (14). The scaling of radius r , baryonic velocities v_k , with $k = \text{disk, bulge, gas}$, and observed velocities v_{obs} under a change of galaxy distance D and inclination angle i are

$$r \rightarrow r' = \frac{D'}{D}r, \quad v_k \rightarrow v'_k = \sqrt{\frac{D'}{D}}v_k, \quad v_{\text{obs}} \rightarrow v'_{\text{obs}} = \frac{\sin(i')}{\sin(i)}v_{\text{obs}}; \quad (\text{A1})$$

Therefore δg_{bar} is independent of distance D and inclination angle i as discussed in e.g. [15], with the resulting scalings of $g_{\text{obs,bar}}(r_j)$ being

$$g_{\text{bar}} \rightarrow g'_{\text{bar}} = g_{\text{bar}}, \quad g_{\text{obs}} \rightarrow g'_{\text{obs}} = \frac{D \sin(i')^2}{D' \sin(i)^2} g_{\text{obs}} \quad (\text{A2})$$

Once we form the ratios $\hat{g}_{\text{bar,obs}}$ then also \hat{g}_{obs} is independent of distance D and inclination angle i such that under a change of distance D and angle i we have

$$\hat{g}'_{\text{bar}} = \hat{g}_{\text{bar}}, \quad \hat{g}'_{\text{obs}} \rightarrow \hat{g}_{\text{obs}} = \hat{g}_{\text{obs}} \quad (\text{A3})$$

We include the systematic uncertainty in \hat{g}_{bar} from the mass to light ratios $\Upsilon_{\text{disk,bulge}}$ via propagation of errors including covariance, such that

$$\begin{aligned} \text{Cov}(f_k, f_l) &= \sum_a \sum_b \frac{\partial f_k}{\partial x_a} \frac{\partial f_l}{\partial x_b} \text{Cov}(x_a, x_b) \\ x_a &= \{\Upsilon_{\text{disk}}, \Upsilon_{\text{bulge}}, v_{\text{gas}}(r_j)\} \\ f_k &= \{g_{\text{bar}}(r_j), g_{\text{obs}}(r_j)\} \end{aligned} \quad (\text{A4})$$

where $\text{Cov}(x_a, x_a) = \delta x_a^2$ is the error of x_a , $\text{Cov}(x_a, x_b) = 0$ for uncorrelated errors $x_{a,b}$, $\text{Cov}(x_a, x_b) = \delta x_a \delta x_b$ for fully correlated errors $x_{a,b}$ and similar for the functions $f_{k,l}$. The functions $f_{k,l}$ are the entire set of accelerations $g_{\text{bar,obs}}(r_j)$ and from this covariance matrix we find the errors on $\hat{g}_{\text{bar,obs}}(r_j)$ and errors on averages $\langle \hat{g}_{\text{bar,obs}}(r_j) \rangle$ which we discuss explicitly below. First the errors $\delta \hat{g}_{\text{bar,obs}}(r_j)$ following from Eq. (A4) are

$$\begin{aligned} \delta \hat{g}_{\text{obs}}(r_j) &= \hat{g}_{\text{obs}}(r_j) \sqrt{\left(\frac{2\delta v_{\text{obs}}(r_j)}{v_{\text{obs}}(r_j)}\right)^2 + \left(\frac{2\delta v_{\text{obs}}(r_{\text{bar}})}{v_{\text{obs}}(r_{\text{bar}})}\right)^2} \quad \text{for } r_j \neq r_{\text{bar}} \\ \delta \hat{g}_{\text{bar}}(r_j) &= \hat{g}_{\text{bar}}(r_j) \sqrt{\left(\frac{2v_{\text{gas}}(r_j)\delta v_{\text{gas}}(r_j)}{v_{\text{bar}}(r_j)^2}\right)^2 + \left(\frac{2v_{\text{gas}}(r_{\text{bar}})\delta v_{\text{gas}}(r_{\text{bar}})}{v_{\text{bar}}(r_{\text{bar}})^2}\right)^2 + (\Delta\Upsilon(r_j))^2}, \quad \text{for } r_j \neq r_{\text{bar}}, \\ \Delta\Upsilon(r_j) &= \sum_{k=\text{disk,bulge}} \delta\Upsilon_k \left(\frac{v_k^2(r_j)}{v_{\text{bar}}^2(r_j)} - \frac{v_k^2(r_{\text{bar}})}{v_{\text{bar}}^2(r_{\text{bar}})}\right) \end{aligned} \quad (\text{A5})$$

while $\delta \hat{g}_{\text{obs}}(r_{\text{bar}}) = \delta \hat{g}_{\text{bar}}(r_{\text{bar}}) = 0$. It follows from Eq. (A5) that $\hat{g}_{\text{bar}}(r_j)$ is insensitive to the systematic uncertainties in $\delta\Upsilon_k$ near r_{bar} by construction, where we are particularly interested in the geometry.

In summary the ratios $\hat{g}_{\text{bar,obs}}$ eliminate the systematic uncertainties in galaxy distance and disk inclination and significantly reduce that from mass to light ratios. These three sources of systematic uncertainties were found to be the dominant sources of scatter in previous analysis of SPARC data

[15]. We have checked explicitly that the error $\Delta\Upsilon$ on $\hat{g}_{\text{bar}}(r_j)$ is indeed small and while we keep it in all error calculations this means we can take $\hat{g}_{\text{obs,bar}}(r_j)$ values from different galaxies to be uncorrelated even if $\delta\Upsilon_k$ are correlated between different galaxies — of course if mass to light ratios between different galaxies vary randomly then so do $\hat{g}_{\text{obs,bar}}(r_j)$ regardless of this residual error being small. While values within a galaxy are still correlated via the same normalization points $\hat{g}_{\text{obs,bar}}(r_{\text{bar}})$.

1. Errors on averages

From the above errors on individual $\hat{g}_{\text{obs,bar}}(r_j)$ the points $\hat{g}_{\text{bar,obs}}(r_{\text{obs}})$ over all galaxies are uncorrelated and their averages and errors presented in Table II are simply given from Eq. A5 by

$$\langle \hat{g}_{\text{bar,obs}}(r_{\text{obs}}) \rangle_{N_{1,2}} = \frac{1}{N_{1,2}} \sum_{j \in N_{1,2}} \hat{g}_{\text{bar,obs}}(r_j), \quad \delta \langle \hat{g}_{\text{bar,obs}} \rangle_{N_{1,2}} = \frac{1}{N_{1,2}} \sqrt{\sum_{r_j \in N_{1,2}} \delta \hat{g}_{\text{bar,obs}}^2}. \quad (\text{A6})$$

The averages and errors on the average of \hat{g}_{obs} (and similarly with \hat{g}_{bar}) for points within a galaxy G can be written as

$$\langle \hat{g}_{\text{obs}} \rangle_G = \frac{1}{N_G} \sum_{j \in G} \hat{g}_{\text{obs}}(r_j), \quad \langle \delta \hat{g}_{\text{obs}} \rangle_G = \frac{1}{N_G} \sqrt{\sum_{r_j \neq r_{\text{bar}}} \left(\hat{g}(r_j) \frac{2\delta V_{\text{obs}}(r_j)}{V_{\text{obs}}(r_j)} \right)^2 + \left(\sum_{r_j \neq r_{\text{bar}}} \hat{g}(r_j) \frac{2\delta V_{\text{obs}}(r_{\text{bar}})}{V_{\text{obs}}(r_{\text{bar}})} \right)^2} \quad (\text{A7})$$

where the error will typically be dominated by the last term, which is $O(1)$ in the number of points N_G while the first term is $O(1/\sqrt{N_G})$ due to the single normalization point in the denominator. To improve on this we also employ the average $g_{\text{bar,obs}}(\Delta r_{\text{bar}})$ for the last results with data set N_3 in table II such that

$$\langle \hat{g}_{\text{bar,obs}} \rangle_{N_3} = \frac{1}{N_G} \sum_{N_G} \frac{N_{\Delta_{\text{bar,G}}}}{N_{\Delta_{\text{obs,G}}}} \hat{g}_{\text{bar,obs}}(\Delta r_{\text{obs}}), \quad (\text{A8})$$

$$\delta \langle \hat{g}_{\text{bar,obs}} \rangle_{N_3} = \frac{1}{N_G} \sqrt{\sum_{N_G} \left(\frac{N_{\Delta_{\text{bar}}}}{N_{\Delta_{\text{obs}}}} \delta \hat{g}_{\text{bar,obs}}(\Delta r_{\text{obs}}) \right)^2} \quad (\text{A9})$$

where again N_G is the number of galaxies used in the average $\Delta r_{\text{bar,obs}}$ are the intervals around $r_{\text{bar,obs}}$ and $N_{\Delta_{\text{obs,G}}}$ are included to correct for cases when either Δr_{bar} or Δr_{obs} contain less than 3 points.

Finally the errors on the binned averages over the points $N_{i,k}^\pm$ in Fig. 4 are computed by first computing the error on the points $G \cap N_{i,k}^\pm$ in $N_{i,k}^\pm$ from a given galaxy G as in Eq. (A7) which then

are uncorrelated between galaxies such that the weighted errors are:

$$\langle \hat{g}_{\text{bar,obs}} \rangle_{N_{i,k}^\pm} = \frac{1}{N_{i,k}^\pm} \sum_{j \in N_{i,k}^\pm} \hat{g}_{\text{bar,obs}}(r_j) \quad (\text{A10})$$

$$\delta \langle \hat{g}_{\text{bar,obs}} \rangle_{N_{i,k}^\pm} = \frac{1}{N_{i,k}^\pm} \sqrt{\sum_G N_{G \cap N_{i,k}^\pm} \delta \langle \hat{g}_{\text{obs}} \rangle_{G \cap N_{i,k}^\pm}^2} \quad (\text{A11})$$

-
- [1] Vera C. Rubin and W. Kent Ford, Jr. Rotation of the Andromeda Nebula from a Spectroscopic Survey of Emission Regions. *Astrophys. J.*, 159:379–403, 1970.
- [2] V. C. Rubin, N. Thonnard, and W. K. Ford, Jr. Rotational properties of 21 SC galaxies with a large range of luminosities and radii, from NGC 4605 /R = 4kpc/ to UGC 2885 /R = 122 kpc/. *Astrophys. J.*, 238:471, 1980.
- [3] A. Bosma. 21-cm line studies of spiral galaxies. 2. The distribution and kinematics of neutral hydrogen in spiral galaxies of various morphological types. *Astron. J.*, 86:1825, 1981.
- [4] F. Zwicky. Die Rotverschiebung von extragalaktischen Nebeln. *Helv. Phys. Acta*, 6:110–127, 1933. [Gen. Rel. Grav.41,207(2009)].
- [5] Douglas Clowe, Marusa Bradac, Anthony H. Gonzalez, Maxim Markevitch, Scott W. Randall, Christine Jones, and Dennis Zaritsky. A direct empirical proof of the existence of dark matter. *Astrophys. J.*, 648:L109–L113, 2006, astro-ph/0608407.
- [6] P. A. R. Ade et al. Planck 2015 results. XIII. Cosmological parameters. *Astron. Astrophys.*, 594:A13, 2016, 1502.01589.
- [7] Ricardo A. Flores and Joel R. Primack. Observational and theoretical constraints on singular dark matter halos. *Astrophys. J.*, 427:L1–4, 1994, astro-ph/9402004.
- [8] B. Moore, S. Ghigna, F. Governato, G. Lake, Thomas R. Quinn, J. Stadel, and P. Tozzi. Dark matter substructure within galactic halos. *Astrophys. J.*, 524:L19–L22, 1999, astro-ph/9907411.
- [9] Michael Boylan-Kolchin, James S. Bullock, and Manoj Kaplinghat. Too big to fail? The puzzling darkness of massive Milky Way subhaloes. *Mon. Not. Roy. Astron. Soc.*, 415:L40, 2011, 1103.0007.
- [10] M. Milgrom. A Modification of the Newtonian dynamics as a possible alternative to the hidden mass hypothesis. *Astrophys. J.*, 270:365–370, 1983.
- [11] Robert H. Sanders and Stacy S. McGaugh. Modified Newtonian dynamics as an alternative to dark matter. *Ann. Rev. Astron. Astrophys.*, 40:263–317, 2002, astro-ph/0204521.
- [12] G. Gentile, B. Famaey, and W. J. G. de Blok. THINGS about MOND. *Astron. Astrophys.*, 527:A76, 2011, 1011.4148.
- [13] Stacy McGaugh, Federico Lelli, and Jim Schombert. Radial Acceleration Relation in Rotationally Supported Galaxies. *Phys. Rev. Lett.*, 117(20):201101, 2016, 1609.05917.
- [14] Federico Lelli, Stacy S. McGaugh, James M. Schombert, and Marcel S. Pawlowski. One Law to Rule

- Them All: The Radial Acceleration Relation of Galaxies. *Astrophys. J.*, 836(2):152, 2017, 1610.08981.
- [15] Pengfei Li, Federico Lelli, Stacy McGaugh, and James Schombert. Fitting the Radial Acceleration Relation to Individual SPARC Galaxies. 2018, 1803.00022.
- [16] R. B. Tully and J. R. Fisher. A New method of determining distances to galaxies. *Astron. Astrophys.*, 54:661–673, 1977.
- [17] Stacy S. McGaugh, Jim M. Schombert, Greg D. Bothun, and W. J. G. de Blok. The Baryonic Tully-Fisher relation. *Astrophys. J.*, 533:L99–L102, 2000, astro-ph/0003001.
- [18] R. H. Sanders. Clusters of galaxies with modified Newtonian dynamics (MOND). *Mon. Not. Roy. Astron. Soc.*, 342:901, 2003, astro-ph/0212293.
- [19] Garry W. Angus, Benoit Famaey, and HongSheng Zhao. Can MOND take a bullet? Analytical comparisons of three versions of MOND beyond spherical symmetry. *Mon. Not. Roy. Astron. Soc.*, 371:138, 2006, astro-ph/0606216.
- [20] Garry W. Angus, HuanYuan Shan, HongSheng Zhao, and Benoit Famaey. On the Law of Gravity, the Mass of Neutrinos and the Proof of Dark Matter. *Astrophys. J.*, 654:L13–L16, 2007, astro-ph/0609125.
- [21] Constantinos Skordis, D. F. Mota, P. G. Ferreira, and C. Boehm. Large Scale Structure in Bekenstein’s theory of relativistic Modified Newtonian Dynamics. *Phys. Rev. Lett.*, 96:011301, 2006, astro-ph/0505519.
- [22] Scott Dodelson and Michele Liguori. Can Cosmic Structure form without Dark Matter? *Phys. Rev. Lett.*, 97:231301, 2006, astro-ph/0608602.
- [23] Scott Dodelson. The Real Problem with MOND. *Int. J. Mod. Phys.*, D20:2749–2753, 2011, 1112.1320.
- [24] Benoit Famaey and Stacy McGaugh. Modified Newtonian Dynamics (MOND): Observational Phenomenology and Relativistic Extensions. *Living Rev. Rel.*, 15:10, 2012, 1112.3960.
- [25] Mordehai Milgrom. Dynamics with a non-standard inertia-acceleration relation: an alternative to dark matter. *Annals Phys.*, 229:384–415, 1994, astro-ph/9303012.
- [26] Benoit Famaey and James Binney. Modified Newtonian dynamics in the Milky Way. *Mon. Not. Roy. Astron. Soc.*, 363:603–608, 2005, astro-ph/0506723.
- [27] J. Bekenstein and Mordehai Milgrom. Does the missing mass problem signal the breakdown of Newtonian gravity? *Astrophys. J.*, 286:7–14, 1984.
- [28] Rafael Brada and Mordehai Milgrom. Exact solutions and approximations of MOND fields of disk galaxies. *Submitted to: Astrophys. J.*, 1994, astro-ph/9407071.
- [29] Julio F. Navarro, Carlos S. Frenk, and Simon D. M. White. A Universal density profile from hierar-

- chical clustering. *Astrophys. J.*, 490:493–508, 1997, astro-ph/9611107.
- [30] Sanders R. H. Mass discrepancies in galaxies - Dark matter and alternatives. *Astronomy and Astrophysics Review*, 2:1–28, 1990.
- [31] Stacy S. McGaugh. The Mass discrepancy - acceleration relation: Disk mass and the dark matter distribution. *Astrophys. J.*, 609:652–666, 2004, astro-ph/0403610.
- [32] J. Janz, M. Cappellari, A. J. Romanowsky, L. Ciotti, A. Alabi, and D. A. Forbes. The mass discrepancy acceleration relation in early-type galaxies: extended mass profiles and the phantom menace to MOND. *Mon. Not. Roy. Astron. Soc.*, 461:2367–2373, September 2016, 1606.05003.
- [33] Olga Chashchina, Robert Foot, and Zurab Silagadze. Radial acceleration relation and dissipative dark matter. *Phys. Rev.*, D95(2):023009, 2017, 1611.02422.
- [34] Douglas Edmonds, Duncan Farrah, Djordje Minic, Y. Jack Ng, and Tatsu Takeuchi. Modified Dark Matter: Relating Dark Energy, Dark Matter and Baryonic Matter. *Int. J. Mod. Phys.*, D27(02):1830001, 2017, 1709.04388.
- [35] De-Chang Dai and Chunyu Lu. Can the Λ CDM model reproduce MOND-like behavior? *Phys. Rev.*, D96(12):124016, 2017, 1712.01654.
- [36] Rong-Gen Cai, Tong-Bo Liu, and Shao-Jiang Wang. Gravitational wave as probe of superfluid dark matter. *Phys. Rev.*, D97(2):023027, 2018, 1710.02425.
- [37] Lasha Berezhiani, Benoit Famaey, and Justin Khoury. Phenomenological consequences of superfluid dark matter with baryon-phonon coupling. 2017, 1711.05748.
- [38] Clare Burrage, Edmund J. Copeland, and Peter Millington. Radial acceleration relation from symmetron fifth forces. *Phys. Rev.*, D95(6):064050, 2017, 1610.07529. [Erratum: *Phys. Rev.*D95,no.12,129902(2017)].
- [39] Erik P. Verlinde. Emergent Gravity and the Dark Universe. *SciPost Phys.*, 2(3):016, 2017, 1611.02269.
- [40] Sunny Vagnozzi. Recovering a MOND-like acceleration law in mimetic gravity. *Class. Quant. Grav.*, 34(18):185006, 2017, 1708.00603.
- [41] Aaron D. Ludlow et al. Mass-Discrepancy Acceleration Relation: A Natural Outcome of Galaxy Formation in Cold Dark Matter Halos. *Phys. Rev. Lett.*, 118(16):161103, 2017, 1610.07663.
- [42] Federico Lelli, Stacy S. McGaugh, and James M. Schombert. SPARC: Mass Models for 175 Disk Galaxies with Spitzer Photometry and Accurate Rotation Curves. *Astron. J.*, 152:157, 2016, 1606.09251.
- [43] K. G. Begeman, A. H. Broeils, and R. H. Sanders. Extended rotation curves of spiral galaxies: Dark haloes and modified dynamics. *Mon. Not. Roy. Astron. Soc.*, 249:523, 1991.

- [44] Jacob D. Bekenstein. Relativistic gravitation theory for the MOND paradigm. *Phys. Rev.*, D70:083509, 2004, astro-ph/0403694. [Erratum: *Phys. Rev.*D71,069901(2005)].
- [45] Stacy McGaugh. Milky Way Mass Models and MOND. *Astrophys. J.*, 683:137–148, 2008, 0804.1314.
- [46] Jonas Petersen and Mads T. Frandsen. Discriminating Between Dark Matter and MOND via Galactic Rotation Curves. 2017, 1710.03096.
- [47] Julio F. Navarro, Carlos S. Frenk, and Simon D. M. White. The Structure of cold dark matter halos. *Astrophys. J.*, 462:563–575, 1996, astro-ph/9508025.
- [48] Julio F. Navarro, Aaron Ludlow, Volker Springel, Jie Wang, Mark Vogelsberger, Simon D. M. White, Adrian Jenkins, Carlos S. Frenk, and Amina Helmi. The Diversity and Similarity of Cold Dark Matter Halos. *Mon. Not. Roy. Astron. Soc.*, 402:21, 2010, 0810.1522.
- [49] Ayuki Kamada, Manoj Kaplinghat, Andrew B. Pace, and Hai-Bo Yu. How the Self-Interacting Dark Matter Model Explains the Diverse Galactic Rotation Curves. *Phys. Rev. Lett.*, 119(11):111102, 2017, 1611.02716.
- [50] Peter Creasey, Omid Sameie, Laura V. Sales, Hai-Bo Yu, Mark Vogelsberger, and Jess Zavala. Spreading out and staying sharp ? creating diverse rotation curves via baryonic and self-interaction effects. *Mon. Not. Roy. Astron. Soc.*, 468(2):2283–2295, 2017, 1612.03903.
- [51] M. Milgrom. A modification of the Newtonian dynamics as a possible alternative to the hidden mass hypothesis. *Astrophys. J.* , 270:365–370, July 1983.
- [52] Pieter van Dokkum et al. A galaxy lacking dark matter. *Nature*, 555(7698):629–632, 2018, 1803.10237.
- [53] B. Famaey, S. McGaugh, and M. Milgrom. MOND and the dynamics of NGC1052-DF2. 2018, 1804.04167.
- [54] Laura Portinari and Paolo Salucci. The structure of spiral galaxies: radial profiles in stellar Mass-to-Light ratio and the Dark Matter distribution. *Astron. Astrophys.*, 521:A82, 2010, 0904.4098.
- [55] Marie-Maude de Denus-Baillargeon, Samuel Boissier, Philippe Amram, Claude Carignan, and Olivier Hernandez. A Galactic Weigh-in: Mass Models of SINGS Galaxies Using Chemo-spectrophotometric Galactic Evolution Models. *Astrophys. J.*, 773:173, 2013, 1307.2516.